Suplemento de la Revista Mexicana de Física **3** 040905 (2022) 1–6

Results on light (anti)nuclei production in Pb–Pb collisions with ALICE at the LHC

Esther Bartsch for the ALICE collaboration

Goethe University Frankfurt, Max-von-Laue-Str. 1, 60438 Frankfurt, Germany

Received 3 July 2022; accepted 15 September 2022

The high collision energies reached at the LHC lead to significant production yields of light (anti)nuclei in proton-proton, p–Pb and Pb–Pb collisions. Light (anti)nuclei are identified using their specific energy loss (dE/dx), measured in the Time Projection Chamber, and their velocity using the Time-Of-Flight detector. The excellent tracking and particle identification capabilities of the ALICE experiment, as well as its low material budget, make this detector unique for measurements of these rarely produced particles. Results on (anti)deuteron, (anti)triton, (anti)^{3}He and (anti)^{4}He production in Pb–Pb collisions at $\sqrt{s_{\rm NN}}$ = 5.02 TeV, including their transverse momentum ($p_{\rm T}$) spectra, production yields and coalescence parameters B_A, are presented. These results will be compared to the expectations of coalescence and statistical hadronization models to obtain information on the production mechanism of light (anti)nuclei in heavy-ion collisions. Furthermore, the first measurements of the $\overline{\rm d}$ and $^3\overline{\rm He}$ absorption cross section are shown.

Keywords: Light (anti)nuclei; transverse-momentum spectra; integrated production yield; statistical hadronization model; coalescence model; absorption cross sections.

1. Introduction

In ultrarelativistic heavy-ion collisions at the Large Hadron Collider (LHC), a state of deconfined strongly interacting matter consisting of quarks and gluons, called the quark-gluon plasma (QGP), is created. Afterwards, the QGP expands and cools down. When the chemical freeze-out temperature is reached the hadron yields are fixed, but there can still be elastic interactions between the particles. After the kinetic freeze-out the momentum spectra of the particles do not change anymore. The abundances of different particle species after hadronization provide information about their production mechanism. Among these particles, light (anti)(hyper)nuclei are of special interest since they are loosely bound objects. Their binding energies are very small compared to the chemical and kinetic freeze-out temperatures and their production mechanism is still not completely understood. There are two classes of models available to describe nuclei production: the statistical hadronization model and the coalescence model (see for instance [1-4], respectively).

In the statistical hadronization or thermal model, the production of nuclei happens before the chemical freeze-out in statistical equilibrium with all other hadrons and scales with the particle mass. In (central) heavy-ion collisions, the system can be described by a grand-canonical ensemble where the free parameters are the average particle number $\langle N \rangle$, the volume V and the temperature T at chemical freeze-out. As the system exchanges particles, the baryochemical potential $\mu_{\rm B}$ has to be introduced to ensure the average conservation of particle numbers. For a certain collision energy, a fit to the measured particle yields can be performed to determine V, T and $\mu_{\rm B}$. However, at LHC energies $\mu_{\rm B}$ is close to zero. For small systems, *i.e.* pp and p-Pb, a canonical approach is used, where the quantum numbers are locally conserved rather than on average, for more details see [2].

In the coalescence model, nuclei are produced at the kinetic freeze-out and the production depends on the wave functions of the nuclear species. They can break apart during the system evolution and be recreated by final state coalescence. A phenomenological parameter of the coalescence model is the coalescence parameter B_A, which is related to the probability to form a nucleus with mass number A via coalescence. It is calculated by the ratio of the invariant yield of a given nucleus to the nucleon invariant yield to the power of A, where the nucleon yield is measured at the corresponding fraction of the nucleus momentum.

Light (anti)(hyper)nuclei are produced at the LHC in pp, p–Pb and, in particular, Pb–Pb collisions. The large high-quality data samples in Pb–Pb collisions at $\sqrt{s_{\rm NN}}$ = 5.02 TeV as well as in pp and p–Pb collisions at several collision energies collected by the ALICE Collaboration provide a unique opportunity to study the production mechanism of these loosely bound objects. Only some of the numerous ALICE results are shown in these proceedings.

Charged-particle multiplicity dependence of $p_{\rm T}$-integrated production yields over the proton yield and of coalescence parameters B_A for $A = 2$ and $A = 3$ nuclei for different collision systems and energies are presented.

Furthermore, the first measurement of the $\overline{\rm d}$ and $^3\overline{\rm He}$ absorption cross sections are shown. It is described how the $^3\overline{\rm He}$ absorption cross section can be used to constrain dark-matter searches.

2. Light nuclei spectra and production yields

Transverse-momentum ($p_{\rm T}$) spectra of several (anti)nuclei (d, t, ^{3}He and ^{4}He) have been measured by ALICE in the high-quality Pb–Pb data sets from 2015 and 2018. The spectra of anti(triton) and (anti)^{4}He are shown in the present work.

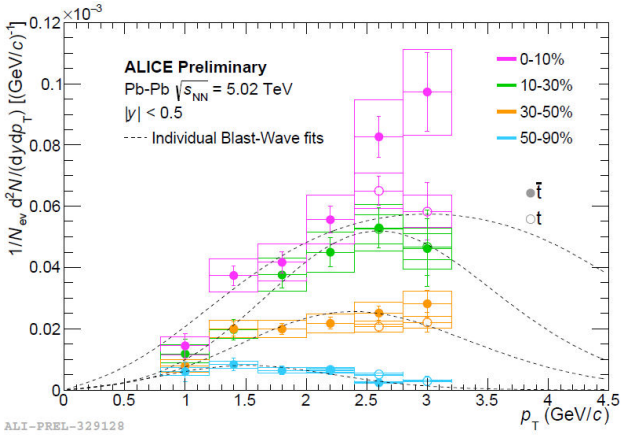

FIGURE 1. p_{T} spectra of (anti)tritons in four centrality intervals together with individual Blast-Wave fits. The $\bar{\mathrm{t}}$ data points are presented by the full circles, whereas the open circles represent the t data points.

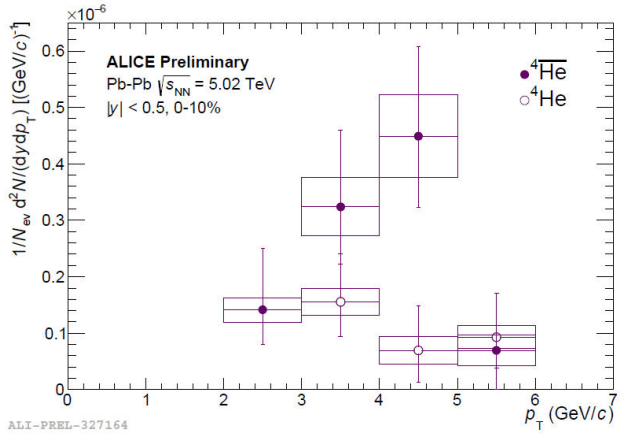

FIGURE 2. p_{T} spectra of (anti)^{4}He in the 0-10% centrality interval. The $^4\overline{\mathrm{He}}$ data points are presented by the full circles, whereas the open circles represent the ^{4}He data points.

The first (anti)triton p_{T} spectra in Pb–Pb collisions at the LHC were obtained from the high-statistics data set from 2018 at $\sqrt{s_{\mathrm{NN}}} = 5.02$ TeV. The nuclei were identified using the energy-loss measurement in the ALICE Time Projection Chamber (TPC), combined with the time-of-flight information provided by the Time-Of-Flight (TOF) detector. The (anti)triton spectra were measured in four centrality intervals (see Fig. 1), where an ordering of the yields can be observed. As there are many knocked-out tritons at low p_{T}, emerging from spallation processes in the beam pipe or the detector material, the triton spectra were only extracted above 2.4 GeV/c (or 2 GeV/c in the most peripheral centrality interval), where this contribution is not present anymore. In the p_{T} overlap region, the measured t and $\bar{\mathrm{t}}$ yields are compatible. The difference in the last two p_{T} bins of the 0-10% centrality interval is less than 2σ. The spectra exhibit an increase of the average p_{T} with increasing centrality and are fitted with individual Blast-Wave functions [5] to extract the integrated production yield dN/dy.

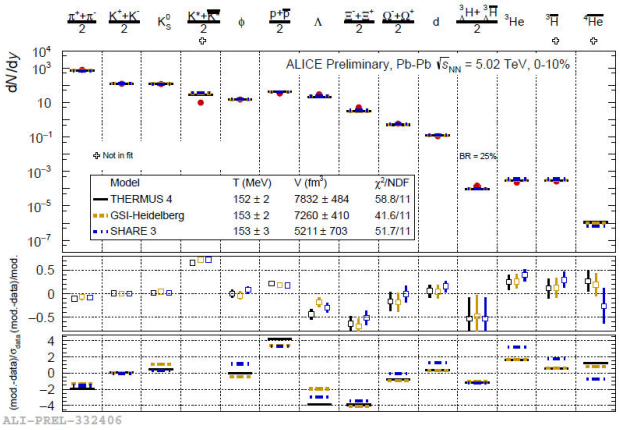

FIGURE 3. p_{T}-integrated production yield dN/dy fitted with three thermal model implementations [7-12] in the 0-10% centrality interval.

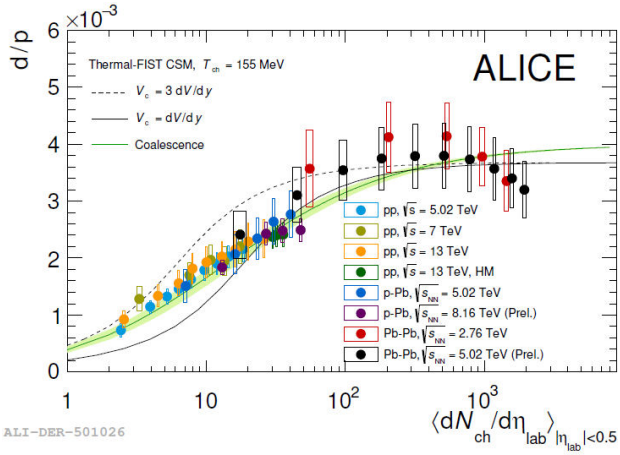

FIGURE 4. Ratio of the p_{T}-integrated production yield of deuterons over the proton production yield versus multiplicity compared to theoretical model predictions.

In the same data set, the first (anti)^{4}He p_{T} spectra were measured (see Fig. 2). These were obtained in the 0-10% most central collisions in four p_{T} bins from 2 to 6 GeV/c for $^4\overline{\mathrm{He}}$ and in three p_{T} bins from 3 to 6 GeV/c for ^{4}He. The ^{4}He spectrum is starting at higher p_{T} for the same reason as for the tritons. The difference between $^4\overline{\mathrm{He}}$ and ^{4}He for $4 < p_{\mathrm{T}} < 5$ GeV/c is about 2σ.

For several particles [6], including light (anti)(hyper)nuclei, the p_{T}-integrated production yield dN/dy was extracted from individual Blast-Wave fits and compared to different versions of the thermal model [7-12] (see Fig. 3). Although the measured $\bar{\mathrm{t}}$ and $^4\overline{\mathrm{He}}$ are not yet included in the fit, the yield is in good agreement with the model predictions from the fit to the other light-flavoured particles.

In addition, the ratio of the p_{T}-integrated yield dN/dy for deuterons (see Fig. 4) as well as ^{3}He and tritons (see Fig. 5) relative to the proton yield has been studied as a function of charged-particle multiplicity $\langle \mathrm{d}N_{\mathrm{ch}}/\mathrm{d}\eta \rangle$ for different collision systems and center-of-mass energies. A universal trend can be observed, showing an increase of the ratio with

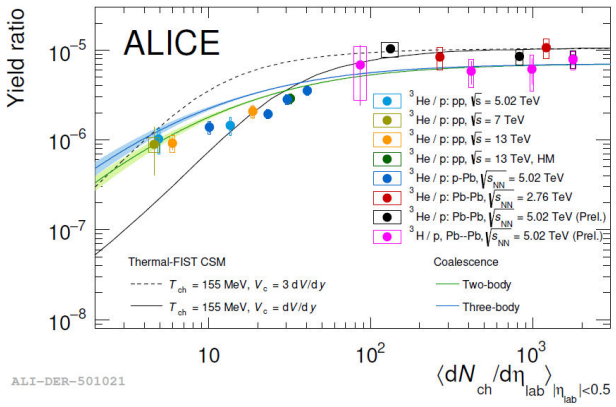

FIGURE 5. Ratio of the p_{T}-integrated production yield of $A = 3$ nuclei over the proton production yield versus multiplicity compared to theoretical model predictions.

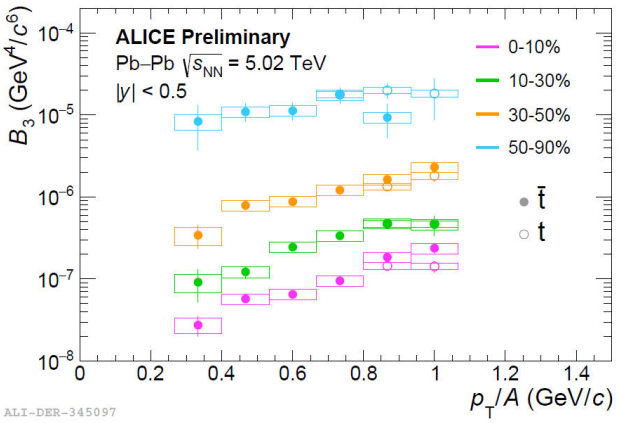

FIGURE 6. B_3 of (anti)tritons in Pb–Pb collisions at 5.02 TeV versus p_{T}/A for several centrality intervals.

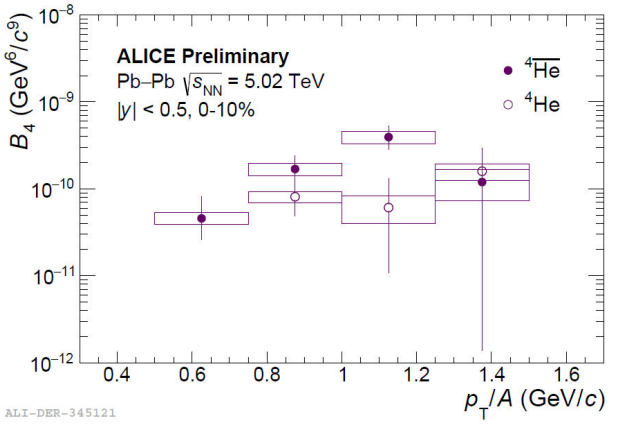

FIGURE 7. B_4 of (anti)^{4}He in Pb–Pb collisions at 5.02 TeV versus p_{T}/A in the 0-10% most central collisions.

increasing multiplicity from pp to p–Pb and a saturation in Pb–Pb collisions. In the d/p case this trend is rather well described by the canonical statistical [13] as well as the coalescence [14] models. In the case of the $A = 3$ nuclei both models have problems to describe the shape of the data at low and intermediate multiplicities. The canonical statistical model is shown for two different correlation volumes V_{c} (dotted and solid black lines). In Fig. 5, two-body and three-body coalescence is shown (green and blue lines, respectively). In two-body coalescence, the coalescence happens between a deuteron and a proton or neutron forming a ^{3}He or t, respectively. In the case of three-body coalescence, the coalescence takes place between two protons and one neutron or two neutrons and one proton.

3. Coalescence parameters

As already mentioned, the probability to form a nucleus via coalescence can be quantified by the coalescence parameter B_A, where A is the mass number of the respective nucleus. Assuming isospin symmetry it can be calculated according to the following expression:

$$B_A = \frac{\frac{1}{2\pi p_{\mathrm{T}}^A}\frac{\mathrm{d}^2 N_A}{\mathrm{d}y\mathrm{d}p_{\mathrm{T}}^A}}{\left(\frac{1}{2\pi p_{\mathrm{T}}^{\mathrm{p}}}\frac{\mathrm{d}^2 N_{\mathrm{p}}}{\mathrm{d}y\mathrm{d}p_{\mathrm{T}}^{\mathrm{p}}}\right)^A} \qquad \text{with } p_{\mathrm{p}} = \frac{p_A}{A} \qquad (1)$$

The invariant yield of a given nucleus is divided by the invariant proton yield to the power of A. It is assumed that neutron and proton yields are the same. The proton yield is measured at the corresponding fraction ($1/2$ for d, $1/3$ for ^{3}He and t, $1/4$ for ^{4}He) of the nucleus momentum.

The B_2 and B_3 are measured for different collision systems and colliding energies and B_4 is measured in Pb–Pb collisions at $\sqrt{s_{\mathrm{NN}}}$ = 5.02 TeV. All three, B_2, B_3 and B_4 are obtained for different values of p_{T}/A. The results on B_3 of (anti)triton obtained in Pb–Pb collisions for different values of p_{T}/A and in different centrality intervals are shown in Fig. 6. It shows a rise with p_{T}/A that becomes milder going from central to more peripheral collisions. The results on B_4 are shown in Fig. 7 for the 0-10% most central collisions, where again a rise of B_4 with p_{T}/A is observed.

To further investigate the production mechanism, it is possible to study the evolution of B_2 and B_3 versus charged-particle multiplicity $\langle \mathrm{d}N_{\mathrm{ch}}/\mathrm{d}\eta\rangle$ for a certain value of p_{T}/A for various collision systems and centre-of-mass energies. This is shown for B_2 at p_{T}/A=0.75 GeV/c and for B_3 of (anti)^{3}He and B_3 of (anti)triton at p_{T}/A=0.73 GeV/c in Figs. 8, 9 and 10, respectively.

All three plots show a smooth evolution with multiplicity across different collision systems. Therefore, the production mechanism seems to depend only on the system size, which can be expressed in terms of the charged-particle multiplicity. At lower multiplicities, where the system size is smaller than the nucleus, a flat behaviour is observed, decreasing slightly from pp to p–Pb collisions, when the system size becomes larger. At higher multiplicities, where the system size is larger than the nucleus, a decreasing trend is observed. The overall trend is described by the coalescence model [15], where in Figs. 8 and 9 two different parametrizations of the source radii (dotted and solid lines) have been applied. The B_3 of (anti)triton (Fig. 10) is also compared to a prediction

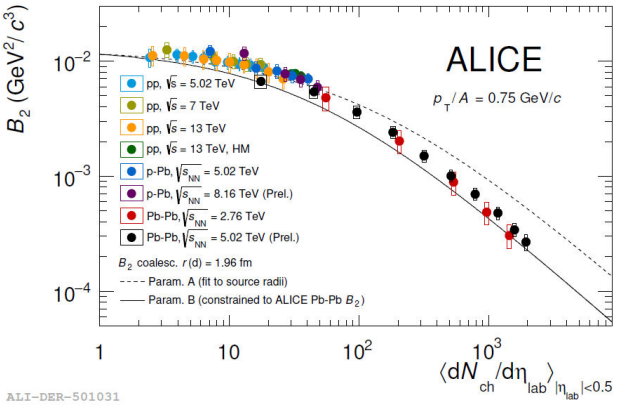

FIGURE 8. Multiplicity dependence of B_2 for different collision systems and energies, compared to the coalescence model for two different parametrizations of the source radii (dotted and solid lines).

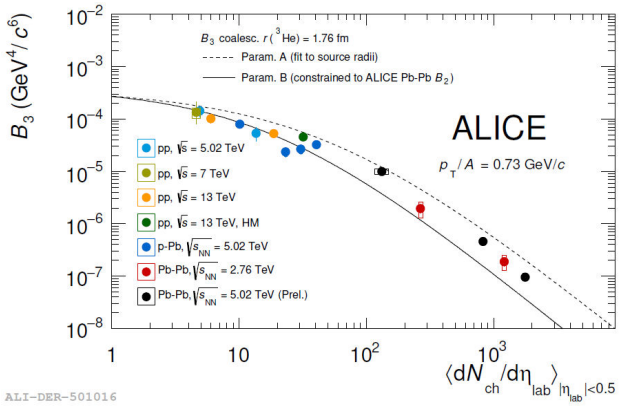

FIGURE 9. Multiplicity dependence of B_3 of (anti)^{3}He for different collision systems and energies compared to the coalescence model for two different parametrizations of the source radii (dotted and solid lines).

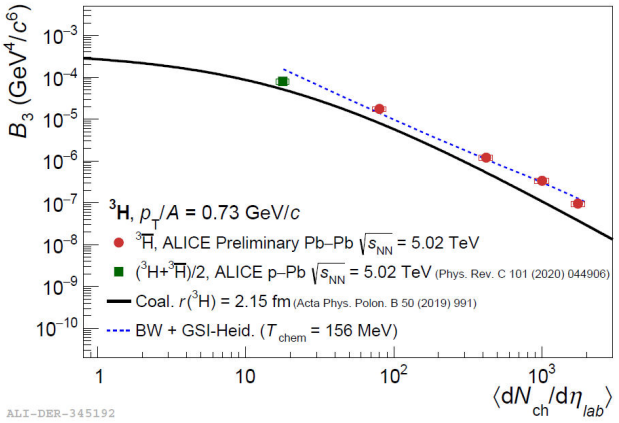

FIGURE 10. Multiplicity dependence of B_3 of (anti)triton for different collision systems and energies compared to coalescence and grand-canonical statistical models.

of the grand-canonical statistical hadronization model (blue dashed line). It appears that no model can describe the values of B_2 and B_3 in the full range of multiplicities studied.

4. Light antinuclei absorption cross section

In this section, the first measurement of the $\overline{\text{d}}$ [16] and $^3\overline{\text{He}}$ [17] absorption cross section is presented. As it is difficult to create an antinuclei beam, no previous measurements are available for $^3\overline{\text{He}}$ and for $\overline{\text{d}}$ measurements are only available in a limited momentum range. In this measurement, the LHC is used as an antimatter factory, while the ALICE detector material is used as a target.

The average mass $\langle A \rangle$ and charge $\langle Z \rangle$ numbers of ALICE are determined by weighting the contribution of the different materials with their density times the length crossed by the particles.

Two alternative methods are employed to determine the antinuclei absorption cross section. For the $\overline{\text{d}}$ in the p–Pb data set at $\sqrt{s} = 5$ TeV and the $^3\overline{\text{He}}$ in the pp data set at $\sqrt{s} = 13$ TeV, the antinuclei yield is compared to the nuclei yield. In this case the average mass number $\langle A \rangle$ is 17.4 if only the TPC is used for the analysis, which is done at low momenta, and 31.8 if a combined analysis with TPC and TOF is performed, which is done at higher momenta.

For the $^3\overline{\text{He}}$ in the Pb–Pb data set at $\sqrt{s_{\text{NN}}} = 5.02$ TeV, the $^3\overline{\text{He}}$ reaching the TOF detector is compared to all reconstructed $^3\overline{\text{He}}$. In this case $\langle A \rangle$ = 34.7, which is the average mass number of the material between TPC and TOF, so the Transition Radiation Detector (TRD), including the support structure.

Figure 11 shows the $^3\overline{\text{He}}$ inelastic cross section measured in the Pb–Pb data sample at $\sqrt{s_{\text{NN}}} = 5.02$ TeV. The measurement is shown with one sigma uncertainty over a wide momentum range from 1 to 10 GeV/c. The dashed line is the default cross section implemented in GEANT4 [18]. One can see, that the measurement is in agreement with the cross section used in GEANT4 within two sigma, however the data suggests a 20-30% smaller cross section. GEANT4 describes

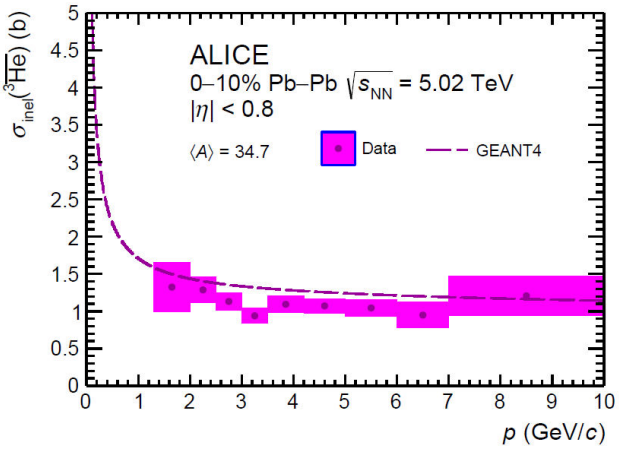

FIGURE 11. Inelastic cross section of $^3\overline{\text{He}}$ measured in Pb–Pb collisions at $\sqrt{s} = 5$ TeV for $\langle A \rangle$ = 34.7 compared to the GEANT4 [18] parametrization.

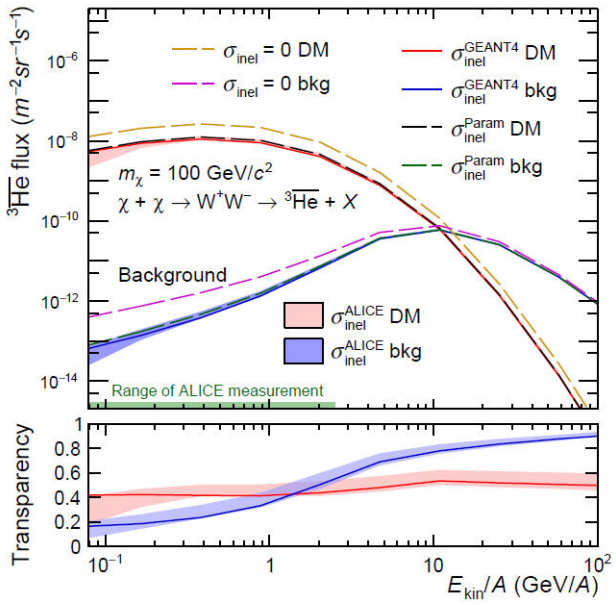

FIGURE 12. $^3\overline{\text{He}}$ flux near earth coming from dark matter annihilation and from cosmic ray interactions for various cases of inelastic cross sections. The lower panel shows the transparency of the galaxy which is the ratio of the flux with and without inelastic processes in GALPROP.

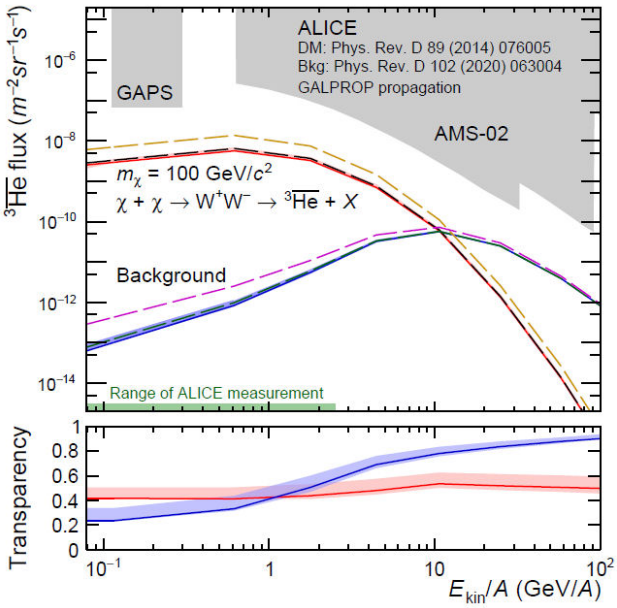

FIGURE 13. $^3\overline{\text{He}}$ flux near earth coming from dark matter annihilation and from cosmic ray interactions for various cases of inelastic cross sections with solar modulation. The lower panel shows the transparency of the galaxy which is the ratio of the flux with and without inelastic processes in GALPROP.

the momentum dependence well and the scale can be calibrated using the data. This is also the case in the other performed cross section measurements.

As $^3\overline{\text{He}}$ is a promising source to discover dark matter particles [19], it is interesting to use the measured $^3\overline{\text{He}}$ absorption cross section to estimate the $^3\overline{\text{He}}$ flux near earth. There are two possible $^3\overline{\text{He}}$ sources considered. One source is the annihilation of a dark matter particle, more precisely a weak-interacting massive particle (WIMP) [19]. In this case the distribution of the flux peaks at low $^3\overline{\text{He}}$ energies. The other source is $^3\overline{\text{He}}$ produced in cosmic ray interactions, which is considered as background. Here the distribution peaks at higher $^3\overline{\text{He}}$ energies. The GALPROP [20] code is used to describe the propagation of the $^3\overline{\text{He}}$ [21] through the galaxy. It includes various contributions like for example a source function, diffusion, convection, fragmentation, decays and inelastic cross sections. The ALICE measurement of the $^3\overline{\text{He}}$ inelastic cross section is implemented in GALPROP.

Figure 12 shows the $^3\overline{\text{He}}$ flux near earth coming from dark-matter particles and from cosmic-ray interactions, which is considered as background, for various cases of inelastic cross sections. One can see that the low energy region is almost free from background for dark-matter searches. The lower panel of Fig 12 shows the transparency of the galaxy which is the ratio of the flux with and without inelastic processes in GALPROP. Figure 13 shows the $^3\overline{\text{He}}$ flux near earth with the solar modulation. Inside the solar system the solar magnetic field is taken into account employing the Force Field approximation. Therefor several species of cosmic rays are used and tuned to match measurements of protons and light nuclei outside and within the solar system. This leads to a shift of high-momentum particles to lower energies. The grey areas in Fig. 13 show the expected sensitivity of the GAPS and AMS-02 experiments. One can see, that these experiments are at the moment not sensitive for the expected $^3\overline{\text{He}}$ fluxes.

5. Conclusion

Results from the high-quality Pb–Pb data sets at a center-of-mass energy of $\sqrt{s_{\rm NN}}$ = 5.02 TeV, collected in 2015 and 2018, have been presented and also been compared to several data sets in other collisions systems.

The $p_{\rm T}$ spectra of various light (anti)nuclei (d, ^{3}He, t, ^{4}He) have been measured. The first $p_{\rm T}$ spectra of $\bar{\rm t}$ and t as well as of $^4\overline{\text{He}}$ and ^{4}He in Pb–Pb at the LHC were shown. The production yields of light nuclei as well as the lighter particles are well described by the thermal model. The production yield ratios of d as well as ^{3}He and t over proton versus multiplicity show an increasing trend going from pp to p–Pb collisions with a saturation in Pb–Pb collisions. For d/p this trend is rather well described by the canonical statistical as well as the coalescence models. For t/p and ^{3}He/p both models have problems in describing the shape at low and intermediate multiplicities. The coalescence parameters B_2, B_3 and B_4 in Pb–Pb collisions exhibit an increase with increasing $p_{\rm T}/A$. This rise becomes milder going from central to more peripheral collisions. Looking at B_2 and B_3 versus multiplicity, which is related to the system size, a clear trend can be observed. At low multiplicities a more flat and slightly decreasing trend going from pp to p–Pb collisions, and at

higher multiplicities a more pronounced decreasing trend is seen. The overall behaviour is described by the coalescence model.

Future data taking periods in 2022-2025 and 2029-2032 will increase the statistics significantly and will hopefully help to solve the current ambiguity between the discussed production models.

Furthermore, the first measurements of the $\overline{\mathrm{d}}$ and $^3\overline{\mathrm{He}}$ absorption cross section were presented. It can be used to determine the $^3\overline{\mathrm{He}}$ flux near earth to perform dark-matter searches, wherefore $^3\overline{\mathrm{He}}$ is a prime candidate. At the moment the determined flux is out of reach for the experiments located in space.

1. A. Andronic, P. Braun-Munzinger, J. Stachel, H. Stöcker, Pro282 duction of light nuclei, hypernuclei and their antiparticles in relativistic nuclear collisions, *Phys. Lett. B* **697** (2011) 203, https://doi.org/10.1016/j.physletb.2011.01.053.
2. B. Dönigus, Light nuclei in the hadron resonance gas, *Int. J. Mod. Phys. E* **29** (2020) 2040001, https://doi.org/10.1142/S0218301320400017.
3. R. Scheibl and U. Heinz, Coalescence and flow in ultrarelativistic heavy ion collisions, *Physical Review C* **59** (1999) 1585, https://doi.org/10.1103/physrevc.59.1585.
4. J. I. Kapusta, Mechanisms for deuteron production in relativistic nuclear collisions, *Phys. Rev. C* **21** (1980) 1301, https://doi.org/10.1103/PhysRevC.21.1301.
5. E. Schnedermann, J. Sollfrank, and U.W. Heinz, Thermal phenomenology of hadrons from 200-A/GeV S+S collisions, *Phys. Rev. C* **48** (1993) 2462, https://doi.org/10.1103/PhysRevC.48.2462.
6. S. Acharya *et al*., (ALICE Collaboration), Production of charged pions, kaons, and (anti-)protons in Pb-Pb and inelastic pp collisions at sNN=5.02 TeV, *Physical Review C* **101** (2020), https://doi.org/10.1103/physrevc.101.044907.
7. S. Wheaton and J. Cleymans, THERMUS: A Thermal model package for ROOT, *Comput. Phys. Commun.* **180** (2009) 84, https://doi.org/10.1016/j.cpc.2008.08.001.
8. A. Andronic, P. Braun-Munzinger, and J. Stachel, Thermal hadron production in relativistic nuclear collisions: The Hadron mass spectrum, the horn, and the QCD phase transition, *Phys. Lett. B* **673** (2009) 142, https://doi.org/10.1016/j.physletb.2009.02.014,10.1016/j.physletb.2009.06.021.
9. A. Andronic *et al*., Decoding the phase structure of QCD via particle production at high energy, *Nature* **561** (2018) 321, https://doi.org/10.1038/s41586-018-0491-6.
10. G. Torrieri *et al*., SHARE: Statistical hadronization with reso313 nances, *Comput. Phys. Commun*. **167** (2005) 229, https://doi.org/10.1016/j.cpc.2005.01.004.
11. G. Torrieri *et al*., SHAREv2: Fluctuations and a comprehensive treatment of decay feed-down, *Comput. Phys. Commun.* **175** (2006) 635, https://doi.org/10.1016/j.cpc.2006.07.010.
12. M. Petran *et al*., SHARE with CHARM, *Comput. Phys. Commun.* **185** (2014) 2056, https://doi.org/10.1016/j.cpc.2014.02.026.
13. V. Vovchenko, B. Dönigus, H. Stöcker, Multiplicity dependence of light nuclei production at LHC energies in the canonical statistical model, *Phys. Lett. B* **785** (2018) 171, https://doi.org/10.1016/j.physletb.2018.08.041.
14. K.-J. Sun, C. M. Ko, B. Dönigus, Suppression of light nuclei production in collisions of small systems at the Large Hadron Collider, *Phys. Lett. B* **792** (2019) 132, https://doi.org/10.1016/j.physletb.2019.03.033.
15. F. Bellini and A. P. Kalweit, Testing production scenarios for (anti-)(hyper-)nuclei and exotica at energies available at the CERN Large Hadron Collider, *Phys. Rev. C* **99** (2019) 054905, https://doi.org/10.1103/PhysRevC.99.054905.
16. S. Achary *et al*., (ALICE Collaboration), Measurement of the low-energy antideuteron inelastic cross section, *Phys. Rev. Lett.* **125** (2020) 162001, https://doi.org/10.1103/PhysRevLett.125.162001.
17. S. Acharya *et al*. (ALICE Collaboration), First measurement of the absorption of $^3\bar{H}e$ nuclei in matter and impact on their propagation in the galaxy (2022).
18. S. Agostinelli *et al.*, GEANT4-a simulation toolkit, Nuclear Instruments and Methods in Physics Research Section A: Accelerators, Spectrometers, *Detectors and Associated Equipment* **506** (2003) 250, https://doi.org/10.1016/S0168-9002(03)01368-8.
19. E. Carlson *et al*., Antihelium from Dark Matter, *Phys. Rev. D* **89** (2014) 076005, https://doi.org/10.1103/PhysRevD.89.076005.
20. A. W. Strong and I. V. Moskalenko, Propagation of cosmicray nucleons in the galaxy, *Astrophys. J.* **509** (1998) 212, https://doi.org/10.1086/306470.
21. Modelling of Antihelium-3 Cosmic-Ray Propagation (2022), https://cds.cern.ch/record/2800897.